Title page

Deterioration mechanism of adhesion properties of FRP-soil interface induced by moisture

Pengchang Wei, PhD, Postdoctoral fellow
Department of Civil and Environmental Engineering, The Hong Kong Polytechnic University, Hong Kong, China;
Email: pengchang.wei@polyu.edu.hk

Zhen-Yu Yin, PhD, Professor (Corresponding author)
Department of Civil and Environmental Engineering, The Hong Kong Polytechnic University, Hong Kong, China;
Research Centre for Nature-based Urban Infrastructure Solutions, The Hong Kong Polytechnic University, Hong Kong, China;
Tel: (+852) 3400 8470; Fax: (+852) 2334 6389;
Email: zhenyu.yin@polyu.edu.hk

Yijie Wang, PhD, Postdoctoral fellow
Department of Civil and Environmental Engineering, The Hong Kong Polytechnic University, Hong Kong, China;
Email: yi-jie.wang@polyu.edu.hk

Fu-Ping Gao, PhD, Professor
Institute of Mechanics, Chinese Academy of Sciences, Beijing, 100190, China;
School of Engineering Science, University of Chinese Academy of Sciences, Beijing, 100049, China;
Email: fpgao@imech.ac.cn

Number of Figures: 15
Number of Tables: 5

Abstract:

The deterioration of FRP-soil interfacial adhesion due to water intrusion has been a core issue in geotechnical engineering, but its microscopic mechanism remains unclear. In this study, molecular dynamics (MD) simulation method is employed to reveal the microscopic deterioration mechanism of water on adhesion properties of epoxy-quartz (i.e., FRP-soil subsystem) interface, the structural and dynamic characteristics of interlayer water film. The steered molecular dynamics (SMD) pulling simulation and the modified Bell's model are used to evaluate the adhesion energy of epoxy-quartz interface in dry and wet cases. The simulation results show that (1) the interfacial water film weakens adhesion strength of epoxy-quartz interface, playing a dual role in "interface isolation" and "lubrication", aggravating the interfacial debonding. (2) The work of adhesion, maximum pulling force, PMF, and adhesion energy of dry system are significantly higher than those of wet system. (3) The interlayer water film has a distinct layered structure: bound, free, and sparse water layers, which have different angle orientations and density distributions. (4) The diffusion coefficient increases with the rising thickness of free water layer, which may trigger a capillary-seepage effect and aggravate interface deterioration. This study provides atomic-scale insights into moisture-induced FRP-soil interface failure mechanism.

Keywords: Adhesion properties; FRP-Soil interface; Molecular Dynamics; Deterioration mechanism; Water intrusion.

1. Introduction

Fiber reinforced polymer (FRP) composites have become the core materials in geotechnical engineering due to their high strength, low weight, corrosion resistance, etc. (Bazli et al. 2021) For example, FRP piles, as a typical application form, are widely used in slope stabilization, foundation reinforcement, and marine engineering, especially in corrosive environments (e.g., seawater erosion, groundwater seepage, etc.) (Abyaneh et al. 2020; Malik et al. 2024). FRP piles have gradually replaced traditional steel piles and concrete piles due to their outstanding properties (Shaia et al. 2018). However, the deterioration of the adhesion properties of FRP-soil interface is the key bottleneck limiting its long-term durability. The water intrusion into the FRP-soil interface could significantly affect their interfacial adhesion strength in long-term water immersion (Fig. 1), resulting in several engineering disasters, such as decreased pile bearing capacity and failure of support structures (Wang et al. 2021; Zhang et al. 2022). Thus, it is necessary to investigate the deterioration mechanism of adhesion properties of FRP-soil interface induced by moisture.

The interfacial mechanical behavior of FRP and soil at the macroscale has usually been studied through experiments, such as direction shear and interface shear tests (Frost and Han 1999; Anagnostopoulos and Papaliangas 2012; Zappalorto et al. 2015; Shaia et al. 2018; Teng et al. 2024; Tian et al. 2024). Tian et al. (2024) investigated the interfacial mechanical behavior of FRP-soil under various cyclic loading, and reported that sand could penetrate and wear the soft FRP due to the difference in hardness between sand and FRP. Shaia et al. (2018) studied the interface friction between FRP and granular materials using a modified shear apparatus, considering particle size and angularity, surface roughness, and applied normal stress. He et al. (2021) studied the tribological and creep-relaxation behavior of sand-FRP under various normal loads. The above studies mainly focus on the mechanical behavior of FRP-soil mixture at the macroscale rather than their interface, while ignoring the effect of interlayer moisture. Furthermore, previous studies have illustrated that the interfacial adhesion between different materials is the combined function of multiple adhesive forces, including

van der Waals forces and electrostatic forces, which are difficult to study using macroscopic and mesoscopic techniques (Wang et al. 2021; Wang et al. 2022; Wei et al. 2024). Therefore, the microscopic mechanism of FRP-soil interface is still unclear, causing a lack of theoretical support for the design of moisture-resistant FRP materials and interface reinforcement strategies.

Molecular dynamics (MD) simulation method is a good approach to reveal the fundamental mechanism of interfacial mechanical behavior of materials at the microscale (Yaphary et al. 2017; Xie et al. 2023; Liu et al. 2024; Niu et al. 2025). The MD model of epoxy-quartz system has been usually established to simulate the FRP-soil system in MD simulations, because quartz and epoxy are one of the main components of soil and FRP, respectively (Xu et al. 2023; Wei et al. 2025). The interfacial friction behavior of epoxy-water-quartz system was investigated using MD simulations (Xu et al. 2023; Wan et al. 2024), which found that the friction coefficient of dry system was significantly greater than that of wet system, where the interlayer water film played a lubricating role. Xie et al. (2022) reported that the interlayer water molecules hindered the interfacial bonding between epoxy and glass fiber through MD simulations. Previous works (Yaphary et al. 2017; Wang et al. 2021) verified that the water solutions weakened the adhesion energy of epoxy-silica interface compared to dry system. The above studies help us deepen our understanding of the interfacial mechanical behavior of epoxy-quartz, but their interfacial adhesion studies at the microscale remain relatively scarce. Moreover, the coupling mechanism of water molecule orientation, diffusion anisotropy, and adhesion energy attenuation has not yet been established, which limits the cross-scale correlation from microscale to macroscopic performance.

This paper systematically investigated the microscale deterioration mechanism of water film on interfacial adhesion properties of epoxy-quartz system (i.e., FRP-soil subsystem) through MD simulation method. The scientific questions to be addressed in this paper are as follows: (1) How does the interlayer water film affect the adhesion properties between quartz and epoxy? (2) What is the layered structure and orientation distribution of the interlayer water film? (3) How does the anisotropy

of water molecule diffusion aggravate the interfacial debonding of quartz and epoxy? To sum up, this paper aims to reveal the mechanism of moisture-induced deterioration of FRP-soil interface adhesion properties, and provide a scientific basis for the development of moisture-resistant FRP composite materials and the reinforcement design of water-sensitive strata.

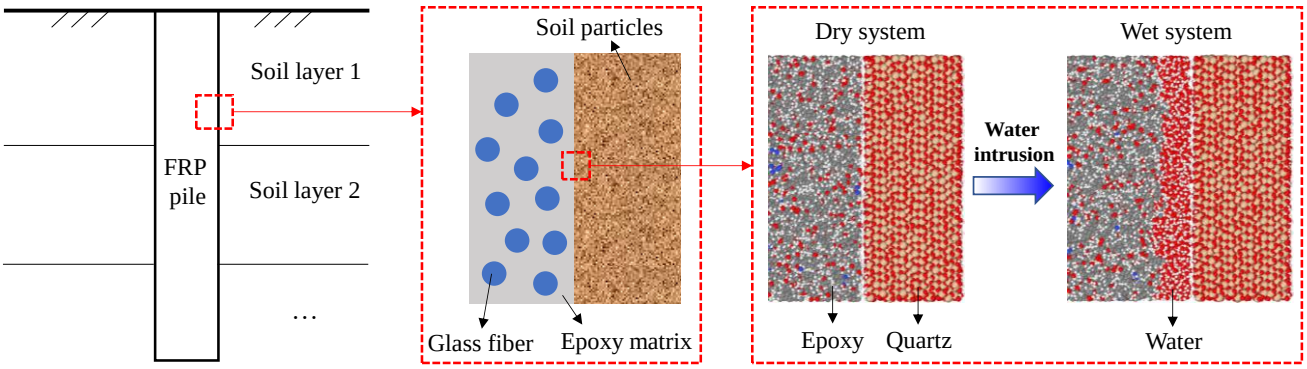

(a) Macroscale (b) Mesoscale (c) Microscale

Fig. 1 Schematic diagram of FRP pile and soil interface from macroscale to microscale.

2. MD simulation process

2.1 MD model setup

Fig. 2 shows the epoxy-quartz and epoxy-water-quartz systems, where the dimensions of the whole system is 76.597 Å × 73.7055 Å × 168.406 Å. The epoxy resin containing 28500 atoms used in this work was derived from our previous work (Wei et al. 2025), which was composed of 500 diglycidyl ether of bisphenol A (DGEBA) and 250 m-phenylenediamine (mPDA), where the conversion percentage of the epoxy resin was 84% (Fig. 2(a)). On the other hand, the atomic structure of quartz with 12960 atoms contained three types of atoms, such as Si, O, and H, where the hydrogen atoms were distributed on the upper and lower surfaces due to the oxidation effect. As shown in Table 1 and Fig. 2(c ~ f), for the epoxy-water-quartz system, various interlayer water film contains various number of water molecules.

As shown in Fig. 2(b), the bottom layer of quartz with a thickness of about 4 Å is set as a fixed layer, where the atoms in this fixed layer are fixed in their initial position during all MD simulations. The upper layer of epoxy with a thickness of about 10 Å was set as a rigid layer (i.e., rigid body), which

was employed in steered molecular dynamics (SMD) pulling process. The atoms outside these above two layers were set as a Newtonian layer, and followed Newton's laws. Moreover, the three layers (i.e., fixed layer, rigid layer, Newtonian layer) were also conducted in epoxy-water-quartz systems (Fig. 2(c ~ f)), where the thickness of the fixed layer and rigid layer were the same.

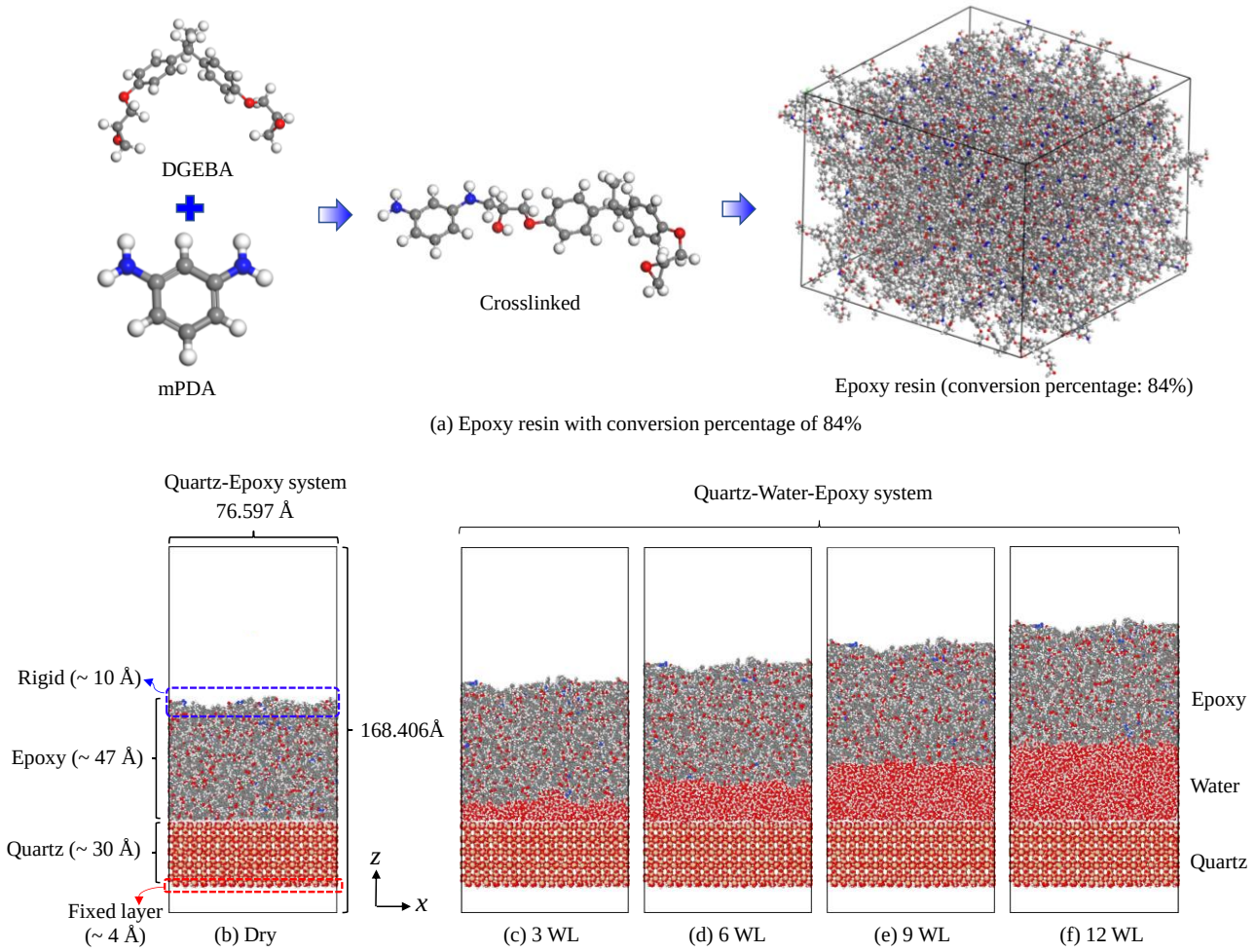

Fig. 2 (a) Epoxy resin with a conversion percentage of 84%, including 500 DGEBA and 250 mPDA. Moreover, the atomic structure of (b) epoxy-quartz system and (c ~ f) various epoxy-water-quartz systems with different water content.

Table 1. Details of MD models used in this study at different water layers (WL), where the thickness of one water layer is around 3.0 Å.

Systems	Number of interlayer water molecules	Thickness of interlayer water film (Å)
Dry	0	0
Wet (3 WL)	4968	9
Wet (6 WL)	9936	18
Wet (9 WL)	14904	27
Wet (12 WL)	19872	36

2.2 Force fields

The Polymer Consistent Force Field (PCFF) and Consistent Valence Force Field (CVFF) force fields were applied to describe the atomistic interaction of epoxy and quartz, respectively. This PCFF-CVFF force fields combination was successfully used to investigate the nanoscale friction and nanoindentation behavior of epoxy-quartz system (Xu et al. 2023; Wei et al. 2025; Wei et al. 2025). The formulas of PCFF and CVFF force fields are shown in Eqs. (1) and (2), respectively.

$$
\begin{aligned}
E_{total} = & \sum_{b}[k_2(b-b_0)^2 + k_3(b-b_0)^2 + k_4(b-b_0)^2] + \sum_{\theta}[H_2(\theta-\theta_0)^2 + H_3(\theta-\theta_0)^2 + H_4(\theta-\theta_0)^2] \\
& + \sum_{\phi}\{V_1[1-cos(\phi-\phi_1^0)] + V_2[1-cos(\phi-\phi_2^0)] + V_3[1-cos(\phi-\phi_3^0)]\} + \sum_{\chi} k_\chi \chi^2 \\
& + \sum_{b}\sum_{b'}(b-b_0)(b'-b'_0) + \sum_{\theta}\sum_{\theta'}(\theta-\theta_0)(\theta'-\theta'_0) + \sum_{b}\sum_{\theta}(b-b_0)(\theta-\theta_0) \\
& + \sum_{b}\sum_{\phi}(b-b_0)(V_1 cos\,\phi + V_2 cos\,2\phi + V_3 cos\,3\phi) \\
& + \sum_{b'}\sum_{\phi}(b'-b'_0)(V_1 cos\,\phi + V_2 cos\,2\phi + V_3 cos\,3\phi) \\
& + \sum_{\theta}\sum_{\phi}(\theta-\theta_0)(V_1 cos\,\phi + V_2 cos\,2\phi + V_3 cos\,3\phi) \\
& + \sum_{\phi}\sum_{\theta}\sum_{\theta'} k_{\phi\theta\theta'} cos\,\phi\,(\theta-\theta_0)(\theta'-\theta'_0) + \frac{e^2}{4\pi\varepsilon_0}\sum_{ij}\frac{q_i q_j}{r_{ij}} + \sum_{ij}\varepsilon_{ij}\left[2\left(\frac{\sigma_{ij}}{r_{ij}}\right)^9 - 3\left(\frac{\sigma_{ij}}{r_{ij}}\right)^6\right]
\end{aligned} \tag{1}
$$

$$
\begin{aligned}
E_{total} = & \sum_{b} D_b\left[1\text{-}e^{-\alpha(b-b_0)}\right] + \sum_{\theta} H_\theta(\theta-\theta_0)^2 + \sum_{\phi} H_\phi[1+s\,cos(n\phi)] + \sum_{\chi} k_\chi \chi^2 \\
& + \sum_{b}\sum_{b'} F_{bb'}(b-b_0)(b'-b'_0) + \sum_{\theta}\sum_{\theta'} F_{\theta\theta'}(\theta-\theta_0)(\theta'-\theta'_0) + \sum_{b}\sum_{\theta} F_{b\theta}(b-b_0)(\theta-\theta_0) \\
& + \sum_{\phi} F_{\phi\theta\theta'} cos\,\phi\,(\theta-\theta_0)(\theta'-\theta'_0) + \sum_{\chi}\sum_{\chi'} F_{\chi\chi'}\chi\chi' + \frac{e^2}{4\pi\varepsilon_0}\sum_{ij}\frac{q_i q_j}{r_{ij}} \\
& + \sum_{ij} 4\varepsilon_{ij}\left[\left(\frac{\sigma_{ij}}{r_{ij}}\right)^{12} - \left(\frac{\sigma_{ij}}{r_{ij}}\right)^6\right]
\end{aligned} \tag{2}
$$

where σ_{ij} and ε_{ij} in Term 13 in Eq. (1) and Term 11 in Eq. (2) are the size and energy parameters between

atoms i and j, respectively. σ_{ij} and ε_{ij} can be calculated through Mixing Lorentz-Berthelot's law (Frenkel and Smit 2001), as the following Eqs. (3) and (4).

$$\sigma_{ij} = \frac{\sigma_i + \sigma_j}{2} \tag{3}$$

$$\varepsilon_{ij} = \sqrt{\varepsilon_i \varepsilon_j} \tag{4}$$

The SPC/E water model (Berendsen et al. 1987) is used to describe the water molecules in this work, where its formula is shown in Eq. (5). The non-bonded interaction between quartz, epoxy, and water molecules contains electrostatic and van der Waals interactions, where the van der Waals interaction of those three materials is calculated by the standard 12-6 Lennard-Jones (LJ) potential. Moreover, a fitting method was proposed in previous work (Wei et al. 2025) to obtain their corresponding 12-6 LJ potential parameters, according to the 9-6 LJ potential parameters in the epoxy system. Table 2 shows the pair interaction potential parameters of the epoxy-water-quartz system.

$$\begin{aligned} E_{\text{total}} &= E_{\text{bond stretch}} + E_{\text{angle bend}} + E_{\text{Coulomb}} + E_{\text{VDW}} \\ &= \sum_{i \neq j} k_1 (r_{ij} - r_0)^2 + \sum_{i \neq j \neq k} k_2 (\theta_{ijk} - \theta_0)^2 + \frac{e^2}{4\pi\varepsilon_0} \sum_{i \neq j} \frac{q_i q_j}{r_{ij}} + \sum_{i \neq j} 4\varepsilon_{ij} \left[\left(\frac{\sigma_{ij}}{r_{ij}} \right)^{12} - \left(\frac{\sigma_{ij}}{r_{ij}} \right)^{6} \right] \end{aligned} \tag{5}$$

Table 2. Pair interaction potential parameters of epoxy-water-quartz system used in this work. (Wei et al. 2025)

Model	lj/cut (12-6 LJ potential)		ε (kcal/mol)	σ (Å)
	atom species	symbol		
Epoxy	carbon in the methyl group	c3	0.056	3.479
	hydrogen, bonded to carbon	hc	0.02	2.589
	generic carbon	c	0.056	3.479
	aromatic carbon	cp	0.066	3.479
	oxygen in ether	oc	0.246	3.065
	carbon bonded to 2 H's	c2	0.056	3.479
	carbon bonded to 1 H	c1	0.056	3.479
	hydroxyl oxygen	oh	0.246	3.065

	carbon in 3-membered ring with hydrogens	c3h	0.056	3.479
	oxygen in 3-membered ring	o3e	0.246	3.065
	hydroxyl hydrogen	ho	0.013	0.949
	nitrogen in aromatic amines	nb	0.065	3.524
	hydrogen bonded to nitrogen	hn	0.013	0.949
	silicon in silicate	sz	0.040	4.053
Quartz	hydroxyl oxygen	oh	0.228	2.860
	hydroxyl hydrogen	ho	0.000	0.000
	oxygen	oz	0.228	2.860
Water	oxygen (SPC/E)	o*	0.1553	3.166
(Berendsen et al. 1987)	hydrogen (SPC/E)	h*	0	0

2.3 Relaxation and simulation details

All MD simulations in this work were performed using the LAMMPS (Plimpton 1995) code. Open Visualization Tool (OVITO) is a specialized visualization tool for MD simulation results, used to dynamically display and analyze molecular structures, as well as Matlab software is used for data processing. Three-dimensional periodic boundary conditions were used for whole system. The SHAKE method was applied to water molecules to improve computational efficiency and maintain molecular structure. The Velocity Verlet algorithm (Frenkel et al. 1997) was used for integrating the motion equations. Moreover, the LJ potential model and PPPM method were employed to calculate the van der Waals interaction and long-range electrostatic interaction, respectively, and their cut-off radius were set as 10 Å and 8 Å. The time step in all MD simulations was 1.0 fs.

To obtain a sufficient equilibrium configuration, the conjugate gradient (CG) method was employed to do the energy minimization for all epoxy-water-quartz systems, where the stopping tolerance for energy and force were set as 1.0e-4 kcal/mol and 1.0e-6 (kcal/mol)/Å, respectively. Moreover, the maximum iterations of the minimizer and the maximum number of force/energy evaluations were 100 and 1000, respectively.

Thereafter, as shown in Fig. 3(a), to obtain a well-balanced system, all whole systems are equilibrated in NVE ensemble and Langevin thermostat at 300 K for 1.0 ns, where the evolution of

total energy with time could be obtained (see Fig. 4(a)). Some key physical quantities in Sections 3.1 ~ 3.4 could be calculated during this stage, such as hydration energy, density distribution of oxygen atom, orientation of pore water, mean square displacement (MSD), work of adhesion, etc.

As shown in Fig. 3(b), the SMD pulling along the *z*-direction for whole systems is employed to investigate their interfacial mechanical properties (see Sections 3.5 and 3.6), where the stiffness coefficient of the virtual spring was set as 100 N/m. The various pulling velocities ranging from 2.5 to 100 m/s were used to study the adhesion energy of whole system. The pulling displacement was set as 30 Å during the pulling process.

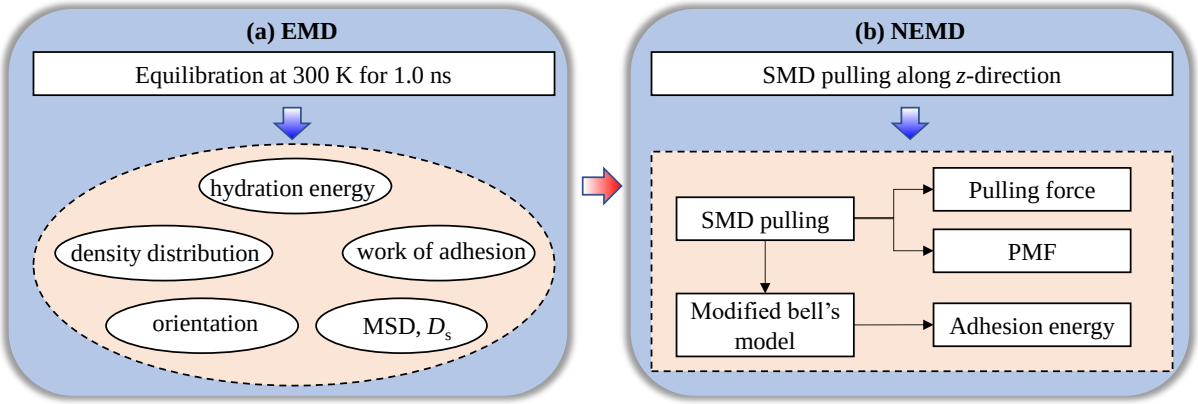

Fig. 3 A flowchart of adhesion study of FRP-soil interface: (a) Equilibrium molecular dynamics (EMD), (b) Non-equilibrium molecular dynamics (NEMD).

3. Results

3.1 Hydration energy

Hydration energy ($\Delta U_H(N)$) is a common important parameter for analyzing the stability of water and soil systems, and belongs to an enthalpy value. It could be obtained by the following equation:

$$\Delta U_H(N) = \frac{U(N) - U(0)}{N} \tag{6}$$

where $U(N)$ is the total energy of a hydrated soil-water system containing water molecules, $U(0)$ is the total energy of a dry soil system, and N is the number of water molecules.

As shown in Fig. 4(a), the evolution of total energy of various systems with time fluctuates around a constant value after 50 ps, indicating that all whole systems are stable. Fig. 4(b) displays that the

hydration energy of various systems decreases with rising interlayer water content, which is related to the interaction between interlayer water molecules and the interaction between interlayer water and solid surfaces. As the interlayer water molecules increase, the interaction between water molecules gradually strengthens, while the interaction between water molecules and the solid surface may gradually weaken, causing a decrease in hydration energy.

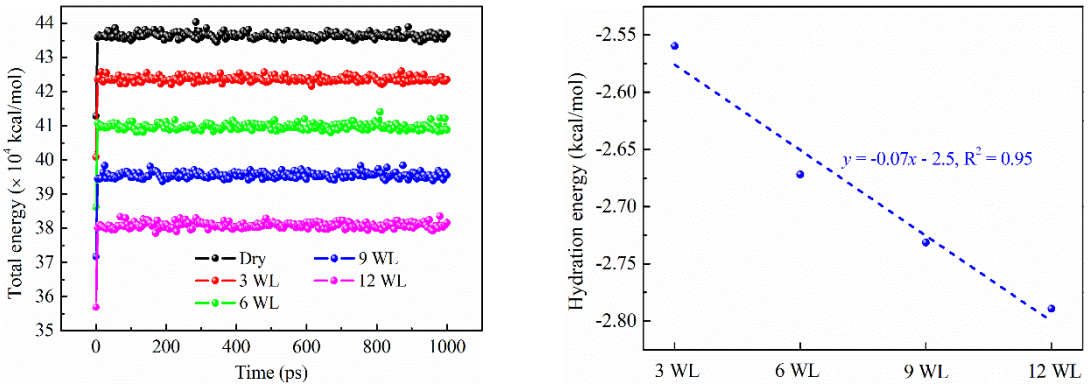

(a) (b)

Fig. 4 (a) Total energy and (b) hydration energy of various systems.

3.2 Atomic density profiles and dynamic properties of interlayer water

As shown in Fig. 5(a, d), the atomic density distribution of oxygen atoms in interlayer water could not only be used to evaluate the hydrophilicity and hydrophobicity of materials, but also to determine the type and thickness of interlayer water (Zhang and Pei 2021), such as bound water, free water, etc. The density of water molecules near quartz surface was higher than 1.0 g/cm^3, showing as bound water. The density of water molecules in the middle fluctuated around 1.0 g/cm^3, showing as free water. However, the density of water molecules near epoxy surface was less than 1.0 g/cm^3. It illustrated that the surface of quartz was hydrophilic, while the surface of epoxy resin was hydrophobic.

As shown in Fig. 5(d, e), all various epoxy-water-quartz systems contain a similar layer structure for interlayer water, where the thickness of the bound water layer in all systems is around 3 Å (i.e., one water layer). The thickness of bound water on clay was usually 3 ~ 6 Å (Zhang and Pei 2021; Wei et al. 2024), where the specific thickness depended on the interfacial properties of soil minerals. The

thickness of the free water layer increases with rising interlayer water content. Moreover, the density of water molecules near the epoxy surface of less than 1.0 g/cm^3 was due to the uneven surface of epoxy-water interface, such as a bottom surface of epoxy and a top surface of interlayer water film (Fig. 5(b, c)).

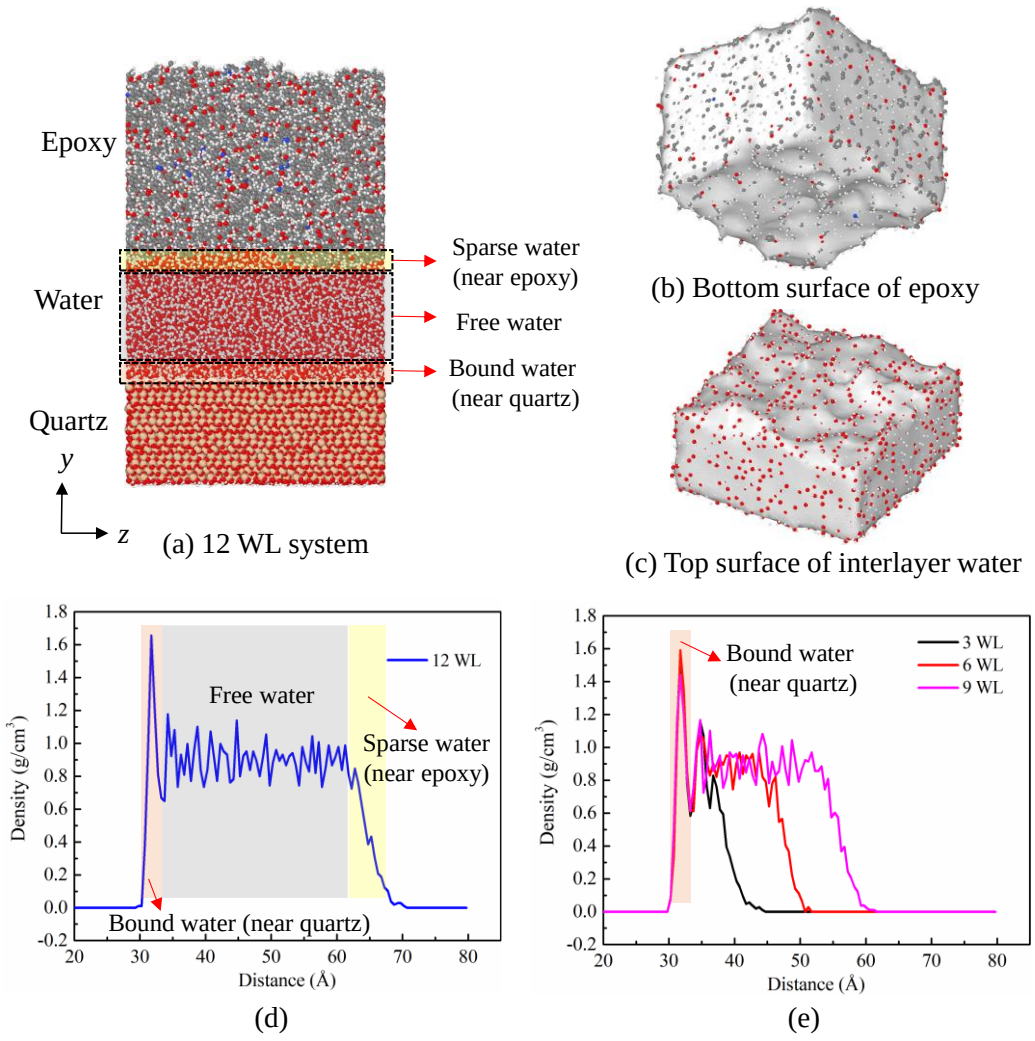

Fig. 5 (a ~ c) Atomistic structure of 12 WL system, including a bottom surface of epoxy and a top surface of interlayer water. Moreover, the density distribution of oxygen atoms in interlayer water molecules for various epoxy-water-quartz systems: (d) 12 WL, (e) 3 ~ 9 WL.

The MSD and diffusion coefficient (D_s) could be calculated by Eq. (7) and (8), respectively.

$$MSD(t) = R^2(t) = \frac{1}{N}\sum_{i=1}^{N}(r_i(t) - r_i(0))^2 \quad (7)$$

$$D_s = \frac{MSD(t)}{2d \times t} \quad (8)$$

where N is the number of interlayer water molecules, $r_i(0)$ and $r_i(t)$ represent the position of atom i at the initial state (t = 0) and time t. Moreover, d denotes the simulation dimension: d = 3 for three-dimensional space (e.g., the overall diffusion coefficient), d = 1 for one-dimensional space (e.g., diffusion coefficient along x-, y-, and z-direction).

To understand the dynamic properties of interlayer water between epoxy and quartz, Fig. 6 and Fig. 7 show the MSD and diffusion coefficient of interlayer water molecules, respectively. As shown in Fig. 7(a), the diffusion coefficient along the x- and y-directions for all wet systems are close, but they are higher than that of the z-direction, indicating that the interlayer water molecules mainly move in the horizontal direction, and their vertical mobility is restricted. This phenomenon was also found in clay-water systems in previous experimental (Dabat et al. 2020) and MD simulation works (Wei et al. 2024), and was significantly related to the spatial confinement of the solid-liquid interface and periodic boundary conditions. As shown in Fig. 2(c-f), the water film in the epoxy-water-quartz system is periodic along the x- and y-directions, allowing water molecules to freely migrate in the horizontal direction, which reflects the diffusion behavior in an infinite system. However, its diffusion behavior along the z-direction is limited by the interface structure between quartz and epoxy resin.

The diffusion coefficient along the z-direction increased with the rising interlayer water layer, while that along the x- and y-direction remained essentially unchanged. Thus, the higher the interlayer water molecules, the higher the number and thickness of the free water layer (Fig. 5), causing the higher the MSD and diffusion coefficient.

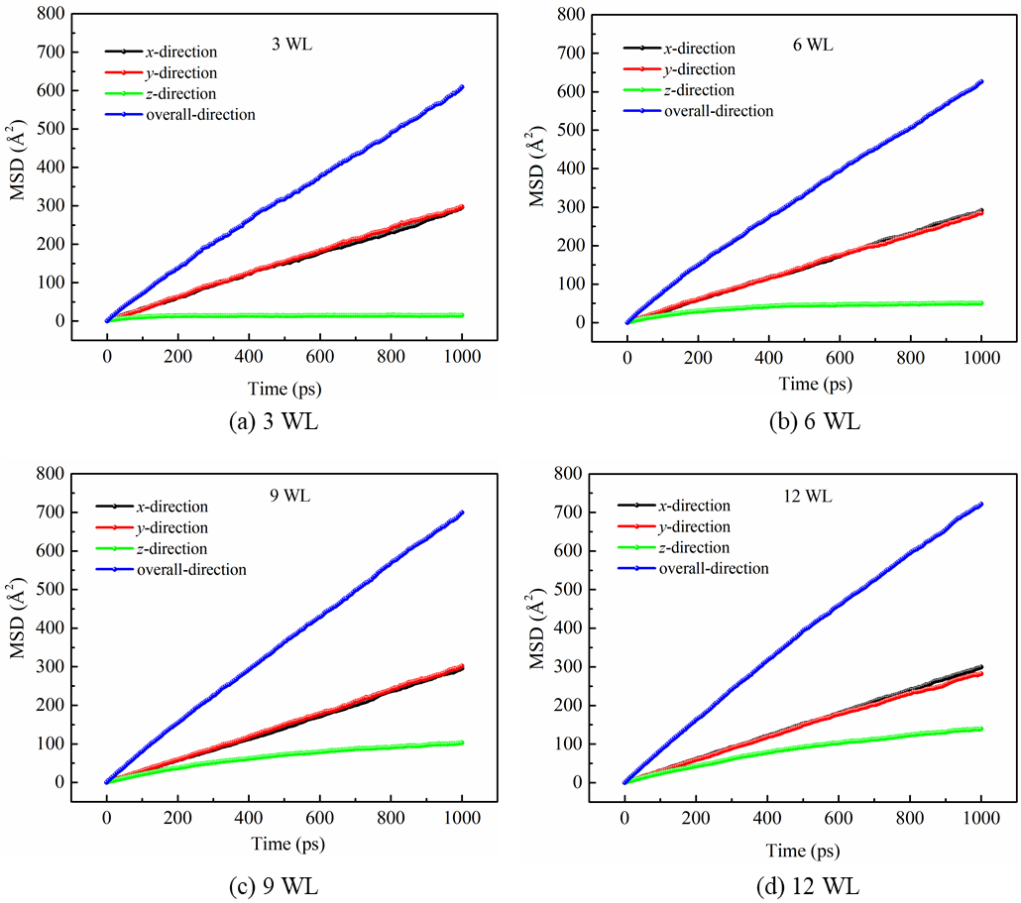

Fig. 6 Mean square displacement (MSD) of interlayer water molecules along different directions in various epoxy-water-quartz systems: (a) 3 WL, (b) 6 WL, (c) 9 WL, (d) 12 WL.

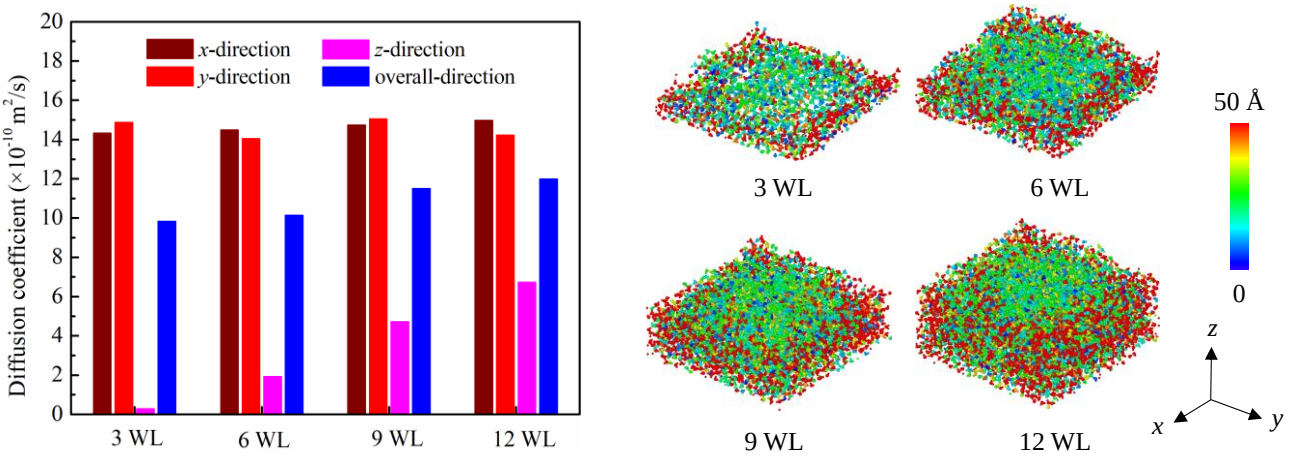

(a) Diffusion coefficient (b) Displacement cloud diagram of water molecules

Fig. 7 (a) Diffusion coefficient and (b) displacement cloud diagram of interlayer water molecules in various epoxy-water-quartz systems.

3.3 The orientation of pore water

To better understand the orientation of pore water molecules in epoxy-water-quartz systems, two key orientational parameters were proposed by Wang et al. (2024) to describe the orientation of water molecules on solid surfaces. As shown in Fig. 8, the first parameter θ_1 is the angle between the bisector of H-O-H angle and the positive direction of the z-axis, and the second parameter θ_2 denotes the angle between the z-axis and the normal vector of the plane formed by three atoms within a water molecule. Moreover, the range of θ_1 and θ_2 were 0° ~ 180° and 0° ~ 90°, respectively. The θ_1 and θ_2 are both equal to 90°, indicating that the water molecule is perpendicular to the soil surface, and θ_2 equal to 0° indicates a parallel arrangement.

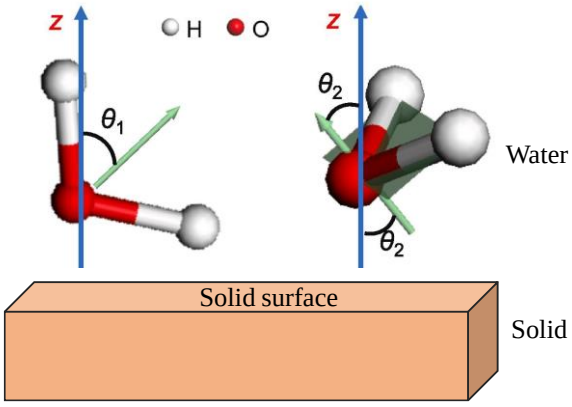

Fig. 8 Illustration of two orientational orderings of water molecules on a solid surface, including two key orientational parameters θ_1 and θ_2. (This figure was modified from previous work (Wang et al. 2024)).

As shown in Fig. 9, the orientational parameters θ_1 and θ_2 of the bound water layer fluctuate significantly, which is due to the effect of hydroxyl group on quartz surface. For the free water layer, the average value of θ_1 and θ_2 fluctuated around 90° and 60° with larger standard deviations, respectively, indicating that the orientation of water molecules gradually transformed to a random distribution, which was consistent with previous MD studies (Wang et al. 2024). Moreover, the orientational parameters of the sparse water layer near epoxy fluctuated significantly, where θ_1

gradually reduced, while θ_2 gradually increased. This was due to the sparse distribution of water molecules in this region (Fig. 5(a-c)), causing limited statistical analysis data.

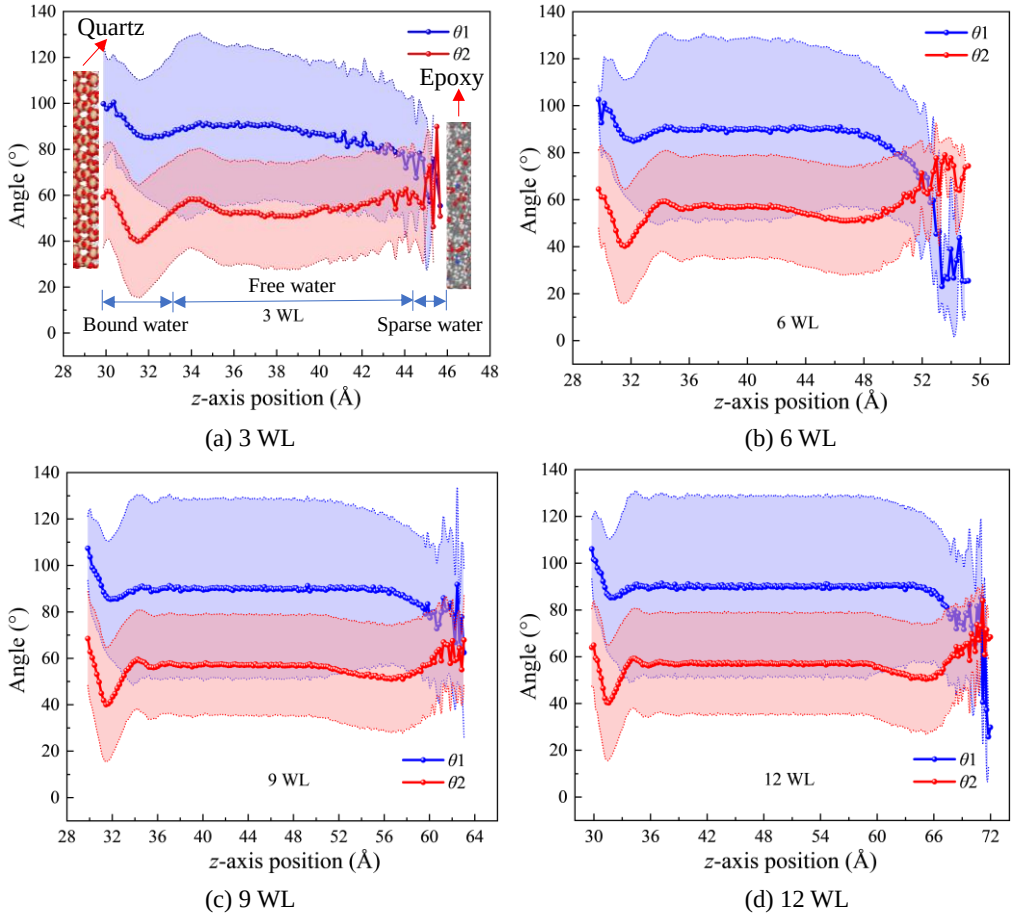

(a) 3 WL (b) 6 WL

(c) 9 WL (d) 12 WL

Fig. 9 Statistical analysis results of the orientation of pore water molecule in various epoxy-water-quartz systems: (a) 3 WL, (b) 6 WL, (c) 9 WL, (d) 12 WL. Moreover, the dashed line in the figure is the standard deviation of the statistical results.

3.4 Work of adhesion and work of debonding

The work of adhesion ($W_{adhesion}$) and work of debonding ($W_{debonding}$) were used to evaluate the interfacial properties of epoxy-quartz interface, where this approach has been successfully applied to polymer-surface systems (Xu and Wang 2016; Bahraq et al. 2022). The work of adhesion was defined as the energy required to separate a unit area of interface into two free surfaces in a vacuum, and was calculated based on the interaction energy (see Eq. (9)). The interaction energy between quartz and

epoxy ($E_{int(epoxy\text{-}quartz)}$) in dry epoxy-quartz system (Fig. 10(a)) was calculated using Eq. (10). The higher value of $W_{adhesion}$ and $E_{int(epoxy\text{-}quartz)}$ implied the greater interaction of interface.

$$W_{adhesion} = \frac{E_{int(quartz-epoxy)}}{A} \tag{9}$$

where $W_{adhesion}$ is the work of adhesion between quartz and epoxy at dry condition, $E_{int(epoxy\text{-}quartz)}$ is the interaction energy between quartz and epoxy in dry epoxy-quartz system, and A is the interface contact area.

$$E_{int(quartz-epoxy)} = E_{quartz-epoxy} - (E_{quartz} + E_{epoxy}) \tag{10}$$

where $E_{int(epoxy\text{-}quartz)}$ is the total energy of dry epoxy-quartz system (see Fig. 10(a)), E_{quartz} is the total energy of quartz system without epoxy, E_{epoxy} is the total energy of epoxy system without quartz. Moreover, for type and source of interaction energy, the van der Waals energy (E_{vdW}) and electrostatic energy ($E_{electrostatic}$) could be calculated in a similar method to Eq. (10).

Fig. 10(a, b) shows a process of how water causes the debonding between quartz and epoxy (i.e., moisture damage). The work of debonding was defined as the work required per unit area to displace epoxy by water on the epoxy-quartz interface (Bahraq et al. 2022), and was calculated through Eq. (11).

$$W_{debonding} = \frac{E_{int(epoxy-water)} + E_{int(quartz-water)} - E_{int(quartz-epoxy)}}{A} \tag{11}$$

where $W_{debonding}$ is the work of debonding at water diffusing into epoxy-quartz interface, where a higher value of $W_{debonding}$ indicates a higher potential for water to cause debonding. $E_{int(epoxy\text{-}water)}$ is the interaction energy between epoxy and water without quartz (Fig. 10(c)), $E_{int(quartz\text{-}water)}$ is the interaction energy between quartz and water without epoxy (Fig. 10(d)), $E_{int(quartz\text{-}epoxy)}$ is the interaction energy between quartz and epoxy at dry condition (Fig. 10(a)). Similarly, for epoxy-water-quartz system, $E_{int(epoxy\text{-}water)}$ and $E_{int(quartz\text{-}water)}$ could be calculated in a similar method to Eq. (10).

To investigate the effect of moisture on the adhesion between two different materials, the energy ratio (ER) has been employed in previous experimental and MD simulation studies (Xu and Wang

2016). ER was the ratio of the work of adhesion at dry conditions to the work of debonding at wet conditions, and was calculated by Eq. (12). The higher the ER value, the more likely it is to indicate a lower susceptibility to moisture damage.

$$\mathrm{ER} = \left| \frac{W_{adhesion}}{W_{debonding}} \right| \tag{12}$$

where W_{adhesion} is the work of adhesion between quartz and epoxy at dry conditions, $W_{\mathrm{debonding}}$ is the work of debonding at water diffusing into epoxy-quartz interface.

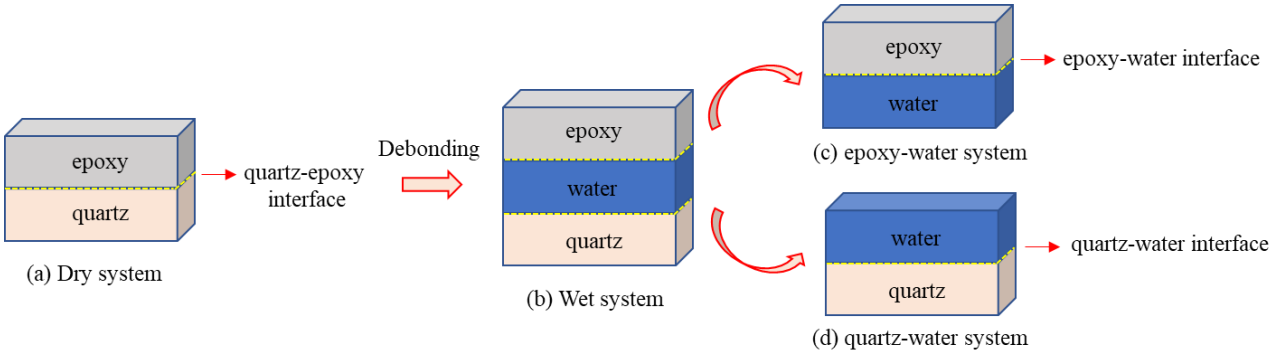

Fig. 10 Idealized representation of quartz/epoxy interface under moisture damage.

Table 3 displays the interaction energy of various interfaces and their contribution to non-bond components (i.e., van der Waals and electrostatic energy), where the value of interaction energy is equal to the summation of van der Waals and electrostatic energy, illustrating that the interaction between quartz and epoxy is mainly composed of the non-bond interaction. Moreover, the value of van der Waals energy was significantly higher than that of electrostatic energy, indicating that the van der Waals energy makes a major contribution to the non-bond interaction energy term.

As shown in Table 3, the work of adhesion of epoxy-quartz interface at dry conditions is higher than all epoxy-water and quartz-water interfaces at wet conditions, further verifying that the water causes significant debonding between the quartz and epoxy interface. Moreover, Fig. 11 shows that the work of debonding and ER of various epoxy-water-quartz systems (3 ~ 12 WL) are close, indicating that the effect of moisture on the adhesion between quartz and epoxy are similar for 3 ~ 12 WL systems.

Table 3. Type and source of interaction energy of different interfaces and their work of adhesion, such as epoxy-quartz interface in epoxy-quartz system, as well as epoxy-water and quartz-water interfaces in epoxy-water-quartz system.

System	Interface type	E_{vdW} (kcal/mol)	$E_{electrostatic}$ (kcal/mol)	E_{total} (kcal/mol)	$W_{adhesion}$ (mJ/m^2)
Dry	$E_{int(epoxy\text{-}quartz)}$	-663.649	-11.349	-674.998	-83.286
3WL	$E_{int(epoxy\text{-}water)}$	-482.771	-125.132	-607.903	-75.008
	$E_{int(quartz\text{-}water)}$	-519.841	8.110	-511.731	-63.141
6WL	$E_{int(epoxy\text{-}water)}$	-502.262	-120.520	-622.782	-76.843
	$E_{int(quartz\text{-}water)}$	-542.750	4.505	-538.245	-66.413
9WL	$E_{int(epoxy\text{-}water)}$	-462.491	-109.980	-572.471	-70.636
	$E_{int(quartz\text{-}water)}$	-545.939	-0.095	-546.034	-67.374
12WL	$E_{int(epoxy\text{-}water)}$	-492.979	-115.230	-608.209	-75.045
	$E_{int(quartz\text{-}water)}$	-498.265	15.754	-482.511	-59.536

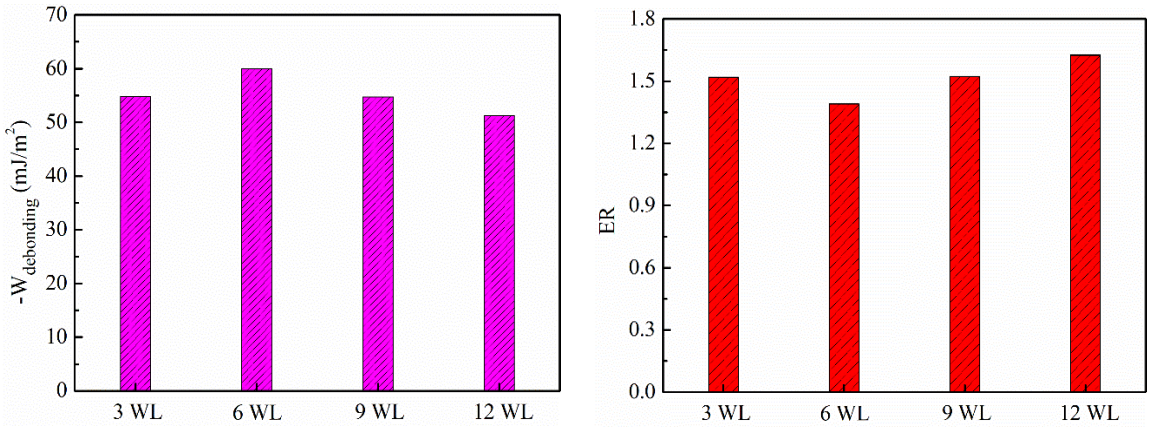

(a) (b)

Fig. 11 (a) Work of debonding ($W_{debonding}$) and (b) ER of various epoxy-water-quartz systems.

3.5 Interfacial mechanical properties

The SMD pulling along the *z*-direction for epoxy-water-quartz system was applied to evaluate their interfacial mechanical properties, where a virtual spring was employed for the rigid group in whole system along the *z*-direction (Fig. 12(a)). The pulling force ($F_{pulling}$) can be calculated by Eq. (13) during the SMD process.

$$F_{pulling} = F_{spring} = K(R - R_0) \quad (13)$$

where F_{spring} is the force of the virtual spring, (R - R_0) is the spring elongation, and K is the stiffness coefficient of the virtual spring (100 N/m in this work).

The potential of mean force (PMF) (Jarzynski 1997) is employed to describe the change of free energy, and could be calculated by Jarzynski's equations:

$$\mathrm{PMF} = -k_B T \, ln\left(\overline{e^{-\frac{W}{k_B T}}}\right) \tag{14}$$

$$W = \int_{r_0}^{r_f} \nabla U_{spring} \cdot d\vec{r} \tag{15}$$

where W, U_{spring}, k_B, and T denote the work and potential energy of the virtual spring, Boltzmann constant, and temperature of whole system, respectively. Moreover, r_t and r_o are the final and initial positions of the slider centroid (i.e., upper layer of epoxy with a thickness of about 10 Å, see Fig. 12(a)).

Fig. 12(b, c) displays the evolution of pulling force and PMF with displacement, where the peak pulling force and PMF of the dry system is higher than that of wet systems (3 ~ 12 WL), which could further verify that the interaction energy of epoxy-quartz interface at dry condition is higher than that at wet condition. Moreover, as shown in Fig. 13(b), the separation layer in epoxy-water-quartz system is the water-epoxy interface during the pulling process, which is mainly due to the hydrophobicity of epoxy.

As shown in Fig. 11 and Fig. 12(b, c), the evolution of pulling force and PMF, the value of work of debonding and ER for 3 ~ 12 WL systems are close, because the thickness of interlayer water film in 3 WL system (~ 9 Å) is around the cutoff radius of non-bonded interaction (i.e., 10 Å), and that in 6 ~ 12 WL system are significantly higher than 10 Å. Therefore, those thick water films could significantly weaken the non-bonded interaction between epoxy and quartz.

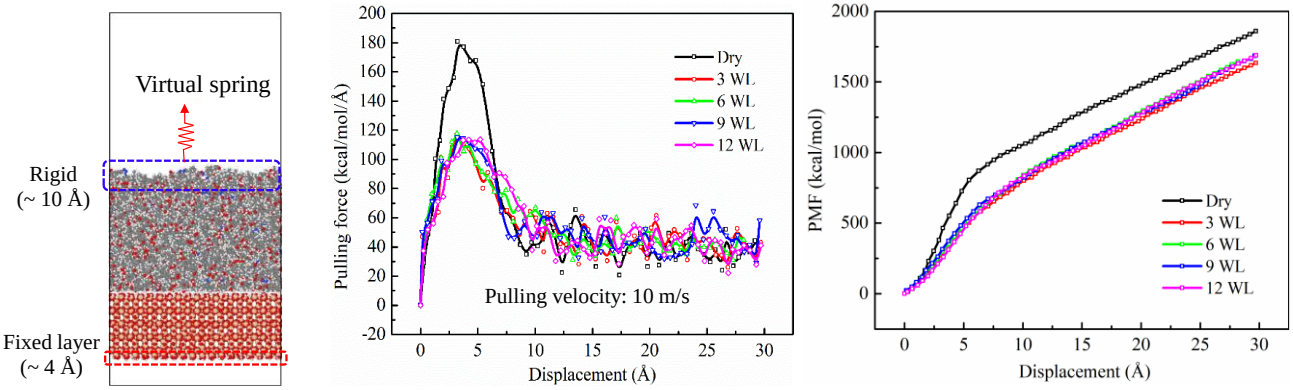

(a) SMD pulling for dry system (b) Pulling force (c) PMF

Fig. 12 (a) Schematic diagram of SMD pulling along *z*-direction for the dry system. Moreover, the evolution of (b) pulling force and (c) potential of mean force (PMF) with displacement for epoxy-quartz and various epoxy-water-quartz systems, where the constant pulling velocity is 10 m/s.

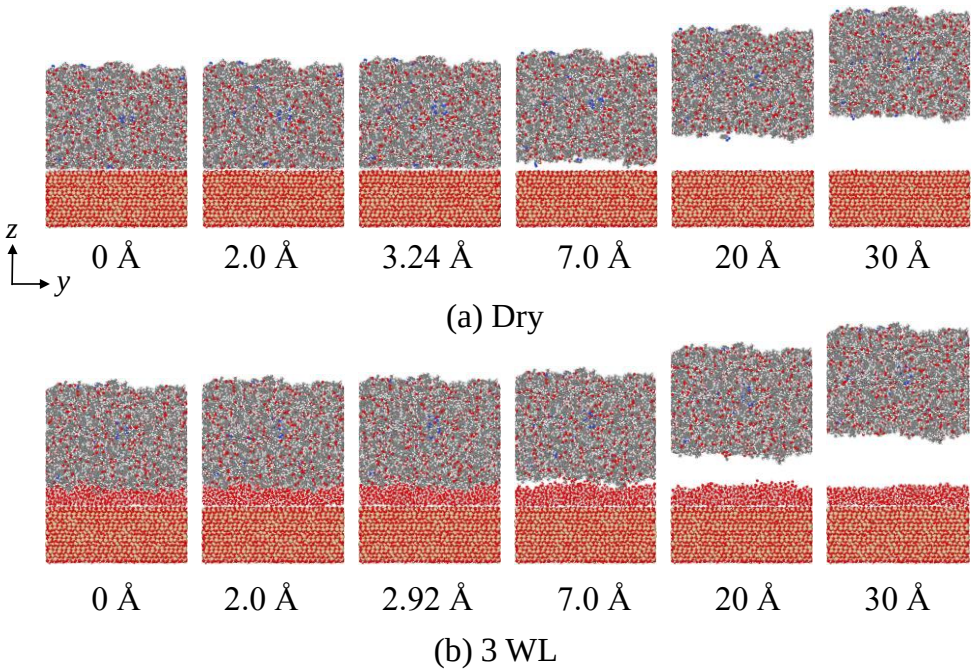

Fig. 13 Evolution of the atomic structure of whole system with different pulling displacements at (a) dry and (b) 3 WL systems.

3.6 Adhesion energy

The adhesion energy (E_b) is usually used to describe the work required to separate two phases from each other. The adhesion energy of whole system could be calculated through the modified Bell's

model (Ackbarow et al. 2007), which was originally proposed by Bell (1978) to investigate the adhesion between cells or between cell and surface. The modified Bell's model could provide the relationship between pulling velocity (v) and maximum pulling force (f) applied to the specific atoms during SMD simulations. The adhesion energy of whole system could be obtained as the following Eqs. (16 ~ 23), where the details of several notations in Eqs. (16 ~ 23) and their definition are shown in Table 4.

$$v = v_0 \cdot \exp\left(\frac{f \cdot x_b}{k_b \cdot T}\right) \tag{16}$$

$$v_0 = w_0 \cdot x_b \cdot \exp\left(-\frac{E_b}{k_b \cdot T}\right) \tag{17}$$

Eq. (18) can be obtained by substituting the v_0 in Eq. (17) into Eq. (16), so that the curve between f and $\ln(v/v^*)$ could be given, where v^* is 1.0 m/s for normalization purposes.

$$f = \left(\frac{k_b \cdot T}{x_b}\right) \ln v - \frac{k_b \cdot T \cdot \ln v_0}{x_b} = A \ln v + B \tag{18}$$

$$A = \frac{k_b \cdot T}{x_b} \tag{19}$$

$$B = -\frac{k_b \cdot T \cdot \ln v_0}{x_b} \tag{20}$$

$$\ln v_0 = -\frac{B}{A} \tag{21}$$

$$x_b = \frac{k_b \cdot T}{A} \tag{22}$$

$$E_b = k_b \cdot T \cdot [\ln(w_0 \cdot x_b) - \ln v_0] \tag{23}$$

Table 4. Details of several notations in Eqs. (16 ~ 23) and their definition.

Notations	Definition	Unit
v	pulling velocity	m/s
v_0	natural bond breaking speed (Bell 1978)	m/s
f	maximum pulling force	kcal/mol/Å
x_b	distance between the equilibrium state and the transition state	Å (or m)
k_b	Boltzmann constant	1.380649×10^{-23} J/K ≈ 1.9872036×10^{-3} kcal/mol/K
T	temperature	K

w_0	a natural vibration frequency	$\approx 1.0 \times 10^{13}$ s^{-1}
E_b	energy barrier between the equilibrium state and the transition state (representing adhesion energy between quartz and epoxy at dry and wet conditions in this work)	kcal/mol

To understand the adhesion properties of epoxy-quartz system at dry and wet conditions, Fig. 14 shows the evolution of pulling force with displacement under various pulling velocities ranging from 2.5 to 100 m/s. Moreover, Fig. 15 shows the linear relationship between maximum pulling force and ln(v/v*) at dry and 3 WL systems, the higher the sliding velocity, the higher the maximum pulling force.

Based on Eq. (18) and the parameters in Fig. 15, Table 5 gives the adhesion energy of dry and 3 WL systems, where their value are 1.658 and 0.867 kcal/mol, respectively. Compared to the dry system, the adhesion energy of the wet (3 WL) system was reduced by 47.7%. This trend in decreasing adhesion energy from dry to wet systems agreed well with previous MD studies (Yaphary et al. 2017; Wang et al. 2021).

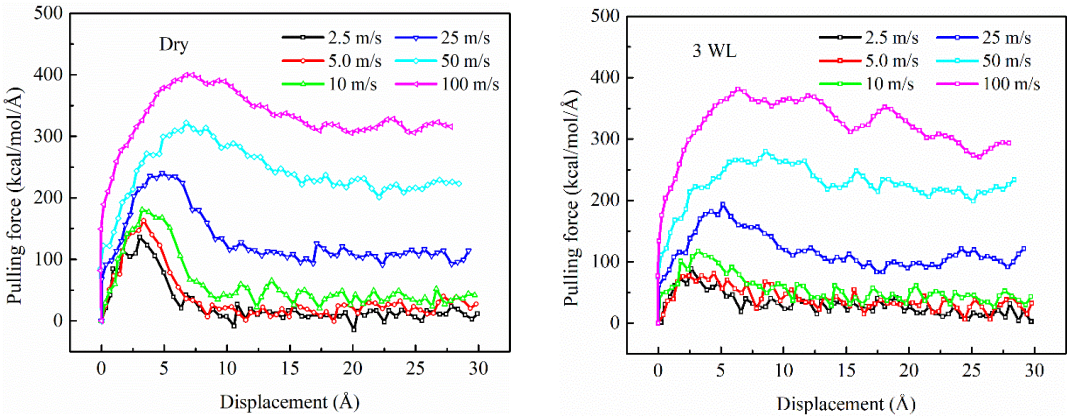

(a) (b)

Fig. 14 Evolution of pulling force with displacement under different pulling velocities (2.5 ~ 100 m/s) at (a) dry and (b) 3 WL systems.

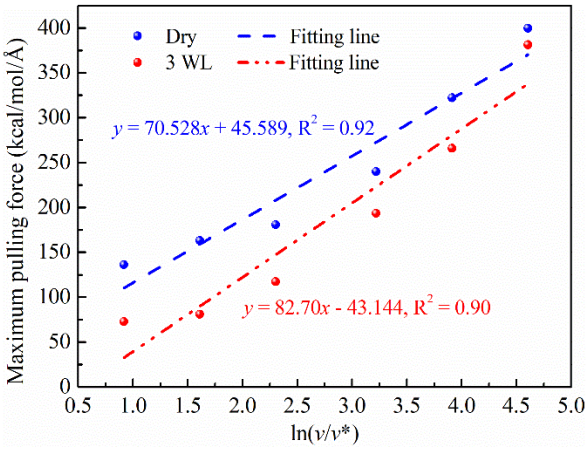

Fig. 15 Relationship between maximum pulling force and ln(v/v^*) at dry and 3 WL systems, where v^* is 1.0 m/s for normalization.

Table 5. Adhesion energy (E_b) of dry and 3 WL systems.

System	A	B	lnv_0 (m/s)	x_b (m)	E_b (kcal/mol)
Dry	70.528	45.589	-0.646	8.45×10^{-13}	1.658
3 WL	82.700	-43.144	0.522	7.21×10^{-13}	0.867

4. Discussion

4.1 Effect of water on the adhesion properties of FRP-soil interface

This MD study reveals the deterioration mechanism of water on adhesion properties of FRP-soil interface. At the microscale, the evolution of hydration energy and interfacial energy with water (Fig. 4) indicates that interlayer water molecules could reduce the interfacial stability by weakening the interaction between quartz and epoxy resin. The work of adhesion (Table 3), maximum pulling force (Fig. 12(b)), and adhesion energy (Table 5) of the dry system (epoxy-quartz) are significantly higher than those of the wet system (quartz-water-epoxy). Because the interlayer water molecules between epoxy and soil can form an interfacial isolation layer, weakening the non-bonded interactions of FRP-soil interface, where the van der Waals interaction is dominant.

The deterioration of adhesion energy from MD simulation can explain the phenomenon commonly observed in geotechnical engineering practice, that is, wet conditions lead to lower bearing capacity of

FRP-soil interface than the peeling failure mode under dry conditions. For example, Xiao et al. (2025) reported that the stress of asphalt mixtures reduced from 0.7 MPa to 0.5 Mpa under high humidity due to moisture damage. Moreover, the maximum pulling force and PMF during the pulling process (Fig. 12) could further confirm that interlayer water molecules act as "lubricants" to promote interfacial separation. This phenomenon is common in widely used epoxy-based adhesives, especially when epoxy interacts with pile surfaces or soil. It also reflects that the deterioration of the macroscopic performance of the FRP-soil system may be caused by changes in its subsystems (i.e., epoxy-quartz system) at lower scales. In engineering practice, this means that in water-rich strata (e.g., clay slopes or groundwater level fluctuation areas) (Ding et al. 2022; Gao et al. 2025), FRP-reinforced structures may fail faster due to the presence of interfacial water films. Thus, it is recommended to design a hydrophobic coating on the FRP surface or use a soil stabilizer to inhibit water from invading key interface areas (Nan et al. 2025).

4.2 Structural and dynamic characteristics of water film

The structural and dynamic properties of the interlayer water film between FRP and soil directly dominate the moisture-induced interfacial deterioration behavior. The atomic density distribution evolution (Fig. 5(d)) shows that the interlayer water film could be stratified: a bound water layer with a thickness of about 3 Å is formed near the quartz surface (density > 1.0 g/cm^3), while a sparse water layer with low density (< 1.0 g/cm^3) is formed near the epoxy surface, and the middle area is free water (density ≈ 1.0 g/cm^3). Moreover, the diffusion coefficient (Fig. 7(a)) further reveals the anisotropy of the movement of water molecules, where the diffusion capacity in the horizontal direction (x/y) is higher than that in the vertical direction (z), which is due to the spatial confinement of the solid-liquid interface and periodic boundary conditions. This asymmetric structure of the interlayer water layer forms a "weakened zone" at the epoxy-quartz interface. The thickness of the free water layer increases with rising interlayer water content (Fig. 5(d, e)), increasing its diffusion coefficient (Fig. 7(a)), which may trigger a capillary-seepage effect and further aggravate interface

deterioration.

The orientation of the interlayer water film (Fig. 9) provides a more in-depth explanation of the deterioration mechanism. The bound water layer near quartz are affected by hydroxyl groups of quartz surface to form a stable hydrogen bond network. Free water molecules are randomly distributed due to thermal motion ($\theta_1 \approx 90°$, $\theta_2 \approx 60°$), while the sparse water layer near epoxy surface has large orientation fluctuations due to their uneven distribution, which weakens the continuity of hydrogen bonds. This orientation heterogeneity directly destroys the synergistic effect of interfacial hydrogen bonds, and reduces the adhesion strength.

To sum up, these studies indicate that the interfacial water has a dual role: (1) acting as a physical barrier to block direct contact between quartz and epoxy resin, reducing their adhesion interaction; (2) acting as a lubricant, exacerbating the interfacial debonding. Bound water enhances interfacial bonding/adhesion strength through hydrogen bonding, while free water weakens shear resistance through lubrication, which is consistent with previous MD work (Wei et al. 2024). Thus, the expansion of the free water layer may induce interfacial delamination in a humid and hot environment, leading to FRP peeling failure.

4.3 Future works

Based on the above research results, some future works are worth conducting as follows:

1) The core purpose of this MD simulation is to reveal the microscopic degradation mechanism of interfacial water molecules, where the interlayer water film (~ nm) in MD simulations is not the same as the capillary water film in the actual project (~ μm). They contain different physical mechanisms, and need to be connected through multi-scale modeling. Thus, combining the coarse-grained MD method and first-principles methods, the mechanism of water molecules weakening interfacial adhesion of FRP-soil at the nano-micro-meso scale could be studied. Moreover, the ReaxFF force field is used to simulate the hydrolysis reaction path and quantify the effect of humidity on the crosslink density of epoxy resin.

2) The soil usually contains multiple components (e.g., clay minerals, organic matter, interlayer ions, etc.), and they have different crystal structures and surface properties. Thus, the synergistic effects of multiple components in soil and FRP interface are worth conducting. Furthermore, the environmental factors (e.g., temperature, PH value, ion concentration, etc.) are necessary to be studied.

3) The hydrophobicity of epoxy resin can be enhanced by adding nanoparticles, such as silica or graphene. The quartz surface is modified with functional groups (e.g., silanization) to introduce chemical bonds to resist moisture corrosion.

4) Machine learning could be used to accelerate the screening of FRP-soil material combinations (e.g., epoxy formulations, soil types) with better moisture resistance, promoting the design of next-generation geotechnical composites for water-sensitive environments.

5. Conclusions

The molecular dynamics (MD) simulation method was used to reveal the deterioration mechanism of water on adhesion properties of the epoxy-quartz (i.e., FRP-soil subsystem) interface at the microscale. The structural and dynamic characteristics of the interlayer water film between FRP and soil were investigated. The steered molecular dynamics (SMD) pulling simulation and modified Bell's model are employed to evaluate the adhesion energy of the epoxy-soil interface in dry and wet cases. The main conclusions in this work are as follows:

1) The invasion of water through the cascade effect of "water film layering structure - hydrogen bonding recombination - diffusion anisotropy of interlayer water - interfacial debonding", which verified the double failure mechanism of water as "lubricant" and "isolation layer". The water could significantly reduce the adhesion strength of epoxy-quartz interface, aggravating the interfacial debonding.

2) The work of adhesion, maximum pulling force, PMF, and adhesion energy of dry system (epoxy-quartz) are significantly higher than those of wet system (quartz-water-epoxy), where

the adhesion energy of wet system (3 WL) decreases by 47.7% compared to dry system.

3) The interlayer water film between FRP and soil has a distinct layered structure: bound water layer (near quartz surface, around 3 Å), free water layer (in the middle), and sparse water layer (near epoxy surface). The bound water layer on the quartz surface forms a stable hydrogen bond network due to the effect of hydroxyl groups, and the sparse water layer on the epoxy surface has large orientation fluctuations due to uneven distribution.

4) The adhesion interaction between quartz and epoxy is composed of the van der Waals and electrostatic interactions, where the contribution of van der Waals interaction is dominant.

5) The thickness of the free water layer increases with rising the interlayer water content, increasing its diffusion coefficient. The diffusion capacity of the interlayer water film in whole system in the horizontal direction (x/y) is higher than that in the vertical direction (z), which is due to the spatial confinement effect of the solid-liquid interface.

This MD study reveals the microscopic deterioration mechanism of water on the FRP-soil interface that cannot be observed in experiments, such as the layering structure of water film, diffusion anisotropy of water, interfacial adhesion mechanism, etc. This study provides an atomic understanding of the adhesion properties of FRP-soil interface induced by moisture. However, the combination of experiments and MD simulations could be better to investigate comprehensively the effect of moisture on the interface properties of FRP-soil at the multiscale, so experiments (e.g., pull-out tests, contact angle measurements, etc.) are worth developing to directly characterize interfacial properties of materials at the macroscale, such as adhesion strength and durability, and verify the reliability of materials in practical environments. Moreover, other future works (see section 4.3) are also worth carrying out.

Acknowledgments

This work was financially supported by the Research Grants Council (RGC) of Hong Kong Special Administrative Region Government (HKSARG) of China (Grant No.: N_PolyU534/20, 15217220),

the National Natural Science Foundation of China (Grant No.: 12061160463).

Data availability

The data used to support the findings of this study are available from the corresponding author upon request.

Author Statement

Pengchang Wei: Conceptualization, Methodology, Investigation, Data Curation, Writing - Review & Editing, Writing - Original Draft, Visualization;

Zhen-Yu Yin: Conceptualization, Writing-Review & Editing, Supervision, Project administration;

Yijie Wang: Methodology, Data Curation, Writing-Review & Editing;

Fu-Ping Gao: Methodology, Writing-Review & Editing.

Competing interests statement

The authors declare no competing financial interests.

References

Abyaneh, M.J., El Naggar, H., and Sadeghian, P. 2020. Numerical modeling of the lateral behavior of concrete-filled frp tube piles in sand. International Journal of Geomechanics, **20**(8). doi: 10.1061/(ASCE)GM.1943-5622.0001725.

Ackbarow, T., Chen, X., Keten, S., and Buehler, M.J. 2007. Hierarchies, multiple energy barriers, and robustness govern the fracture mechanics of α-helical and β-sheet protein domains. Proceedings of the National Academy of Sciences of the United States of America, **104**(42): 16410-16415.

Anagnostopoulos, C.A., and Papaliangas, T.T. 2012. Experimental investigation of epoxy resin and sand mixes. Journal of Geotechnical and Geoenvironmental Engineering, **138**(7): 841-849. doi: 10.1061/(ASCE)GT.1943-5606.0000648.

Bahraq, A.A., Obot, I.B., Al-Osta, M.A., Baghabra Al-Amoudi, O.S., and Maslehuddin, M. 2022. Molecular-level investigation on the effect of surface moisture on the bonding behavior of cement-epoxy interface. Journal of Building Engineering, **61**: 105299. doi: 10.1016/j.jobe.2022.105299.

Bazli, M., Heitzmann, M., and Hernandez, B.V. 2021. Hybrid fibre reinforced polymer and seawater sea sand concrete structures: a systematic review on short-term and long-term structural performance. Construction and Building Materials, **301**: 124335. doi: 10.1016/j.conbuildmat.2021.124335.

Bell, G.I. 1978. Models for the specific adhesion of cells to cells. Science, **200**(4342): 618-627. doi: 10.1126/science.347575.

Berendsen, H.J.C., Grigera, J.R., and Straatsma, T.P. 1987. The missing term in effective pair potentials. The Journal of Physical Chemistry, **91**(24): 6269-6271. doi: 10.1021/j100308a038.

Dabat, T., Porion, P., Hubert, F., Paineau, E., Dazas, B., Grégoire, B., Tertre, E., Delville, A., and Ferrage, E. 2020.

Influence of preferred orientation of clay particles on the diffusion of water in kaolinite porous media at constant porosity. Applied Clay Science, **184**: 105354. doi: 10.1016/j.clay.2019.105354.

Ding, X., Luo, Z., and Ou, Q. 2022. Mechanical property and deformation behavior of geogrid reinforced calcareous sand. Geotextiles and Geomembranes, **50**(4): 618-631. doi: 10.1016/j.geotexmem.2022.03.002.

Frenkel, D., Smit, B., Tobochnik, J., McKay, S.R., and Christian, W. 1997. Understanding molecular simulation. Computers in Physics, **11**(4): 351. doi: 10.1063/1.4822570.

Frenkel, D., and Smit, B. 2001. Understanding molecular simulation: from algorithms to applications. Academic Press.

Frost, J.D., and Han, J. 1999. Behavior of interfaces between fiber-reinforced polymers and sands. Journal of Geotechnical and Geoenvironmental Engineering, **125**(8): 633-640. doi: 10.1061/(ASCE)1090-0241(1999)125:8(633).

Gao, Z., Kong, L., Wang, S., Wang, G., and Yan, J. 2025. The infiltration characteristics of expansive soil subjected to drying–wetting cycles under surcharge. Canadian Geotechnical Journal, **62**: 1-16. doi: 10.1139/cgj-2023-0223.

He, H., Chen, W., Yin, Z., Senetakis, K., and Yin, J. 2021. A micromechanical-based study on the tribological and creep-relaxation behavior of sand-frp composite interfaces. Composite Structures, **275**: 114423. doi: 10.1016/j.compstruct.2021.114423.

Jarzynski, C. 1997. Nonequilibrium equality for free energy differences. Physical Review Letters, **78**(14): 2690-2693. doi: 10.1103/PhysRevLett.78.2690.

Liu, Y., Zheng, Y., Lin, H., Wei, P., Fan, Q., Huang, G., and Meng, D. 2024. Calculation of contact angle via young-dupré equation with molecular dynamic simulation: kaolinite as an example. Colloids and Surfaces A: Physicochemical and Engineering Aspects, **697**: 134469. doi: 10.1016/j.colsurfa.2024.134469.

Malik, N., Chen, W., Chen, Z., Wu, P., and Yin, J. 2024. Axial cyclic and static behavior of frp composite seawater–sea sand concrete piles ended in a rock socket. Journal of Geotechnical and Geoenvironmental Engineering, **150**(4). doi: 10.1061/JGGEFK.GTENG-11529.

Nan, J., Chang, D., Liu, J., Feng, L., Lee, J., and Li, X. 2025. Investigation on the micro–macro properties of ionic soil stabilizer and inorganic materials treated saline soil. Acta Geotechnica. doi: 10.1007/s11440-025-02721-9.

Niu, W., Zheng, Y., Yin, Z., Yao, C., and Wei, P. 2025. Multiscale mechanical behavior of hydrated expansive soil: insights from experimental and md study. Computers and Geotechnics, **181**: 107129. doi: 10.1016/j.compgeo.2025.107129.

Plimpton, S. 1995. Fast paraller algorithms for short-range molecular dynamics. Journal of Computational Physics, **117**: 1-19. doi: 10.1006/jcph.1995.1039.

Shaia, H.A., Al-Asadi, A.K., and Ramadan, S.H. 2018. Evaluation of the interface friction between fiber-reinforced polymers and granular materials using modified shear apparatus. International Journal of Civil Engineering and Technology, **9**(13): 1010-1016.

Teng, J.C., Yin, Z.Y., Chen, W.B., Song, D.B., and Dai, J.G. 2024. Interface shear behavior of sandy soil-frp with epoxy hardness effect and abrasion. Journal of Composites for Construction, **28**(6).

Tian, Y., Li, S., Yin, Z., and Senetakis, K. 2024. A micromechanical study on sand − frp interface subjected to cyclic loading. Composite Structures, **346**: 118452. doi: 10.1016/j.compstruct.2024.118452.

Wan, J., Zaoui, A., Li, X., and Zheng, Y. 2024. Molecular dynamics simulations of the interface friction behavior between fiber-reinforced polymer pile and sand. Tribology International, **192**: 109288. doi: 10.1016/j.triboint.2024.109288.

Wang, P., Yin, Z., Zhou, W., and Chen, W. 2022. Micro-mechanical analysis of soil-structure interface behavior under

constant normal stiffness condition with dem. Acta Geotechnica, **17**(7): 2711-2733. doi: 10.1007/s11440-021-01374-8.

Wang, X.Q., Jian, W., Buyukozturk, O., Leung, C.K.Y., and Lau, D. 2021. Degradation of epoxy/glass interface in hygrothermal environment: an atomistic investigation. Composites. Part B, Engineering, **206**: 108534. doi: 10.1016/j.compositesb.2020.108534.

Wang, Y., Hu, L., and Yin, Z. 2024. Effects of micropores on the vapor sorption isotherm and structural parameters characterization of kaolinite. Computers and Geotechnics, **172**: 106453. doi: 10.1016/j.compgeo.2024.106453.

Wei, P., Yin, Z., Hicher, P., and Xu, W. 2025. Interfacial mechanical behavior of epoxy-quartz: md nanoindentation and nanoscratching study. Acta Geotechnica, **20**(4): 1599-1620. doi: 10.1007/s11440-024-02503-9.

Wei, P., Yin, Z., Yao, C., Ren, Z., Zheng, Y., and Ma, W. 2024. Atomistic origin of montmorillonite clay subjected to freeze-thaw hysteresis. Journal of Rock Mechanics and Geotechnical Engineering. doi: 10.1016/j.jrmge.2024.11.004.

Wei, P., Yin, Z.Y., Hicher, P.Y., and Zheng, Y. 2025. Molecular dynamics study on quartz‐indenter shape and depth effects in epoxy interfacial mechanics. International Journal for Numerical and Analytical Methods in Geomechanics. doi: 10.1002/nag.4021.

Wei, P., Zhou, S., Zheng, Y., Yin, Z., and Xu, W. 2024. Nanoscale stick-slip behavior and hydration of hydrated illite clay. Computers and Geotechnics, **166**: 105976. doi: 10.1016/j.compgeo.2023.105976.

Xiao, Z., Quan, W., Smirnov, I., and You, L. 2025. Integrated experimental-computational approach for three-stage creep characterization of asphalt mixtures under coupled high temperature-humidity loading. Computers & Structures, **315**: 107794. doi: 10.1016/j.compstruc.2025.107794.

Xie, H., Liu, Y., Long, Z., Xu, F., You, L., Tang, X., Zhu, C., and Ding, Y. 2023. Micro-characterization of the adhesion properties and mechanisms at the asphalt-silica aggregate interface under combined thermal-oxygen aging and chloride salt erosion. Construction & building materials, **401**: 132818. doi: 10.1016/j.conbuildmat.2023.132818.

Xie, J., Chen, K., Yan, M., Guo, J., Xie, Q., and Lü, F. 2022. Effect of temperature and water penetration on the interfacial bond between epoxy resin and glass fiber: a molecular dynamics study. Journal of Molecular Liquids, **350**: 118424. doi: 10.1016/j.molliq.2021.118424.

Xu, G., and Wang, H. 2016. Study of cohesion and adhesion properties of asphalt concrete with molecular dynamics simulation. Computational Materials Science, **112**: 161-169. doi: 10.1016/j.commatsci.2015.10.024.

Xu, W.Q., Yin, Z.Y., and Zheng, Y.Y. 2023. Frp‐soil interfacial mechanical properties with molecular dynamics simulations: insights into friction and creep behavior. International Journal for Numerical and Analytical Methods in Geomechanics. doi: 10.1002/nag.3607.

Yaphary, Y.L., Yu, Z., Lam, R.H.W., Hui, D., and Lau, D. 2017. Molecular dynamics simulations on adhesion of epoxy-silica interface in salt environment. Composites Part B: Engineering, **131**: 165-172. doi: 10.1016/j.compositesb.2017.07.038.

Zappalorto, M., Pontefisso, A., Fabrizi, A., and Quaresimin, M. 2015. Mechanical behaviour of epoxy/silica nanocomposites: experiments and modelling. Composites Part A: Applied Science and Manufacturing, **72**: 58-64. doi: 10.1016/j.compositesa.2015.01.027.

Zhang, K., Zhang, Q., and Xiao, J. 2022. Durability of frp bars and frp bar reinforced seawater sea sand concrete structures in marine environments. Construction and Building Materials, **350**: 128898. doi: 10.1016/j.conbuildmat.2022.128898.

Zhang, S., and Pei, H. 2021. Determining the bound water content of montmorillonite from molecular simulations. Engineering Geology, **294**: 106353. doi: 10.1016/j.enggeo.2021.106353.